Chapter 5

Effect of Calcium Substitution on Structure and Electrical Properties

5.1 Introduction

Increasing interest in the synergistic effects on the properties of HEOs has been a driving force for designing and examining systems with five or more components. This has resulted in the development of several novel systems with specific properties [46,116,145]. It was initially suggested that an increase in ΔS_{mix} of an equiatomic multi-element alloy might favour the single-phase formation over competing intermetallic phases [10,11,51,86]; however, experiments revealed that in many cases, configuration entropy could not overcome the contrasting driving force i.e. enthalpy [49,52,83,97,151]. Therefore, a high entropy does not guarantee the single solid solution phase formation. For the single-solid solution stabilisation, $T\Delta S$ should be enough to more than compensate for the positive enthalpy term [45]. Incorporating a greater number of components could theoretically boost the configurational entropy, enhancing single-phase stabilization. However, this benefit is contingent up on avoiding microstates, any ordering effects, or defect proliferation that might lower involving enthalpy [46,83]. Additionally, maintaining structural electroneutrality, whether through accommodating larger cations or creating vacancies, must remain energetically viable. Since each ion in a

perfect crystal occupies a specific symmetry site within the unit cell, a substitutional ion having a comparable size and charge can occupy lattice positions with little disruption. The size difference between the host ion and substitutional ion causes strain in the lattice [19,201,202]; as a result, ions in crystal lattice shift their position until all the neighbouring ions experience zero force. Several studies indicate that adding cations of varying sizes changes the stabilization temperature of the high entropy phase [23,29,49,59]. However, no systematic study has been undertaken to quantify the effect of strain due to the addition of cations of varying radii on the phase stability of HEOs.

Further, the electrical properties of HEOs, especially their exceptional dielectric behaviour, have captured the spotlight in modern materials research [1,2,91,145,157]. With the surge in demand for high-dielectric-constant materials, HEOs stand out as promising candidates for advanced energy storage applications. Notably, rocksalt-structured HEOs demonstrate colossal dielectric constants (CDC), offering the exciting possibility of tuning their properties by simply adjusting the composition of their constituent elements.

In the present work, Ca^{2+} having significantly different ionic radii, is substituted in the equiatomic quinary (Mg,Co,Ni,Cu,Zn)O to synthesise single phase $(Mg,Co,Ni,Cu,Zn)_{1-x}Ca_xO$ (x = 0.05, 0.1, 0.16) HEO using solution combustion synthesis (SCS) route [119,187]. A simple model is utilized to quantify the strain [203,204] and its effect on the stabilization temperature. The fine structure and distortion in the structure due to Ca^{2+} substitution is studied by extended X-ray absorption spectroscopy (EXAFS) and transmission electron microscopy (TEM).

The frequency-dependent dielectric response and electrical conductivity were analysed using impedance spectroscopy.

5.2 Experimental

5.2.1 Materials preparation

Solution combustion synthesis (SCS) was utilised (discussed in Chapter 3) for preparing (Mg,Co,Ni,Cu,Zn)O, and Ca^{2+} added HEO sample, i.e. $(Mg,Co,Ni,Cu,Zn)_{1-x}Ca_xO$ (x = 0.05, 0.1,0.16). Citric acid was utilised as a fuel, resulting in fluffy powders, which were then calcined in the temperature range of 1000°C-1400 °C to achieve a single phase. For ease of presentation, compositions (Mg,Co,Ni,Cu,Zn)O, $(Mg,Co,Ni,Cu,Zn)_{0.95}Ca_{0.05}O$, $(Mg,Co,Ni,Cu,Zn)_{0.9}Ca_{0.1}O$, and (Mg,Co,Ni,Cu,Zn,Ca)O will hereafter be denoted as TM-HEO0, TM-HEO5, TM-HEO10 and TM-HEO16, respectively. To characterize the dielectric properties and electrical conductivity the powders were pelletized and sintered. The as-synthesized TM-HEO0 and TM-HEO10 powders were ground and blended with a 5% polyvinyl alcohol (PVA) solution using an agate mortar. The resulting mixture was uniaxially pelletized into disks measuring 10 mm in diameter and 2.5 ± 0.2 mm in thickness, achieving a green density of approximately 49.27%. The green compacts were then sintered in a tubular furnace (ANTS Ceramics Pvt. Ltd., India) following a two-stage heating process: an initial hold at 600°C for 2 hours to eliminate the binder, followed by sintering at 1100°C for 4 hours to achieve >90% relative density.

5.2.2 Characterization

XRD patterns were recorded over a 2θ range of 20°–80° at a scan rate of 2°/min and a step size of 0.02°. Samples for TEM imaging were prepared by dispersing the powder in ethanol through ultrasonication for 90 min, followed by drop-casting on a 200-mesh carbon-coated Cu grid. XPS was carried out to ascertain the oxidation state of the elements while the binding energies were calibrated against the C1s peak at 284.8 eV. To ensure accurate results, the possibility of surface contamination was eliminated by sputtering the sample with argon (Ar) for 20 seconds before XPS measurement. X-ray absorption spectroscopy (XAS) was employed to investigate the fine structure of the powders. K-edge absorption energies were aligned with metal foil references, and oxide standards were used for calibration. Each scan was averaged over three repetitions. Scattering pathways were modelled using FEFF6, and data analysis and fitting were conducted with the Demeter® software suite. The dielectric properties and impedance spectroscopy of the samples were assessed using a frequency LCR meter (Keysight, model E4980A/AL, Malaysia) operating within the 10 Hz–1 MHz range at three temperatures: 303 K, 363 K, and 423 K.

5.3 Results and discussion

5.3.1 Effect of strain on stabilizing temperature

The strain due to the larger Ca^{2+} cation substitution in (Mg,Co,Ni,Cu,Zn)O has been shown to influence the formation of single-phase and change the phase stability landscape [49]. The strain ε due to a larger cation (Ca^{2+}) substitution is described by [203] :

$$\varepsilon = \frac{\partial r}{r} \qquad (1)$$

$$\varepsilon = \frac{\overline{r}_1 - \overline{r}_0}{\overline{r}_0} \qquad (2)$$

where $\overline{r}_0, and\ \overline{r}_1$ are the average ionic radius of the base HEO cations and Ca^{2+} substituted six component HEO, respectively. The effective radius of Ca^{2+} substituted HEO at different substitution concentrations is calculated by using relation [205].

$$\overline{r}_1 = \sum_{i=1}^{6}(n_i . r_i) \qquad (3)$$

where $n_i , and\ r_i$ are the molar concentration of constituent cations and their ionic radius, respectively. **Figure 5.1(a)** shows the schematic of the crystal structure of five component rocksalt HEO. Since in the rocksalt structure, cations and anions are arranged in a cubic lattice, volumetric strain is determined by the relation [19]:

$$\varepsilon_v = \frac{\partial V}{V} = 3\frac{\partial a}{a} \qquad (4)$$

$$\varepsilon_v = \frac{3(a_{sub} - a_{par})}{a_{par}} \qquad (5)$$

where a_{sub}, and a_{par} are the lattice parameters of Ca^{2+} substituted HEO and the parent TM-HEO0, respectively. For equation (4), it was assumed that the lattice experiences a hydrostatic state of strain. **Figure 5.1(b)** shows how ionic size mismatch creates local strain in the lattice. For estimating strain energy stored in the lattice due to the substitution of larger size Ca^{2+} into the lattice of the five-

element HEOs, it was assumed that TM-HEO0 experiencing negligible strain (as ionic radii of the TM cations are nearly the same; 0.69-0.72 Å) and taken as reference. The strain energy equivalent to the local elastic pressure for the structural decomposition is calculated from the lattice strain model proposed by Brice et al. [203,206,207]

$$U = 4\pi E N_A \left(\frac{\overline{r}_0}{2}(\overline{r}_1 - \overline{r}_0)^2 + \frac{1}{3}(\overline{r}_1 - \overline{r}_0)^3\right) \quad (6)$$

where U is the strain energy in kJmol^{-1}, E is Young's modulus of the HEO (108GPa) [208], $\overline{r}_0, and\ \overline{r}_1$ are the average ionic radii of cations in five-component TM-HEO0, and Ca^{2+} added six-component HEOs, respectively. **Figure 5.1(c)** depicts a plot of strain energy due to Ca^{2+} cation substitution. This strain energy is added to the enthalpy of mixing (ΔH) to calculate the critical temperature beyond which ΔG become negative for the single-phase formation [209]. Thus, it is evaluated that strain energy increases on increasing Ca^{2+} concentration, which in turn enhances the enthalpy of mixing. In addition to the strain effect, the enthalpy penalty (ΔH) for $(Mg,Co,Ni,Cu,Zn)_{1-x}Ca_xO$ (x = 0.05, 0.1, 0.16) system involves enthalpy change associated with the phase transition of ZnO (wurtzite to rocksalt) and CuO (tenorite to rocksalt). The enthalpy associated with the phase transition to rocksalt for ZnO and CuO was reported to be around 25 kJmol^{-1} and 22 kJmol^{-1}, respectively [5, 29]. The crystal structure of CaO (sixth constituent) is also the same (i.e rocksalt) with a slightly different lattice parameter (4.80 ± 0.005 Å) from the HEOs (4.23 Å ± 0.007). There is only a volume misfit in the case of CaO, and doesn't involve significant enthalpy change associated with the structural transition. For simplicity, we assumed that the solution of each binary oxide into rocksalt is ideal. To account

for the structural transition of ZnO and CuO, enthalpic penalties were calculated based on a product of the mole fractions of each component multiplied by reference transition enthalpy, including the strain effect. Thus, the overall driving force (ΔH) can be formulated as:

$$\Delta H = U_{Ca^{2+}} + x_i(25) + y_i(22) \quad \text{kJ·mol}^{-1} \qquad (7)$$

where x_i, y_i represent the molar composition of ZnO and CuO, respectively. The configurational entropy of parent equiatomic HEO (Mg,Co,Ni,Cu,Zn)O and Ca^{2+} added HEOs are calculated using the relation [211]:

$$\Delta S_{config.} = -R\left(\sum_{i=1}^{n} x_i \ln x_i\right)_{cation} \qquad (8)$$

Phase formation is governed by the minimization of Gibbs free energy which is connected to the enthalpy *ΔH* and entropy *ΔS*, through the equation [212,213]

$$\Delta G = \Delta H - T\Delta S \qquad (9)$$

It is obvious that in the case ΔH > 0, the entropy term (TΔS) should be high enough to surpass the enthalpy penalty so that ΔG becomes negative for single-phase formation [45]. Since the configuration entropy for the random solid solution phase is constant, it can be stable above a critical temperature (T_{cr}). **Figure 5.1 (d)** shows variation in the estimated critical temperature for varying Ca^{2+} substitution. The estimated critical temperature increases with the calcium addition. The critical temperature increases from 848 ℃ for the parent TM-HEO0 to 957, 1043, and 1359 ℃ for TM-HEO5, TM-HEO10 and TM-HEO16, respectively (**Table 5.1**).

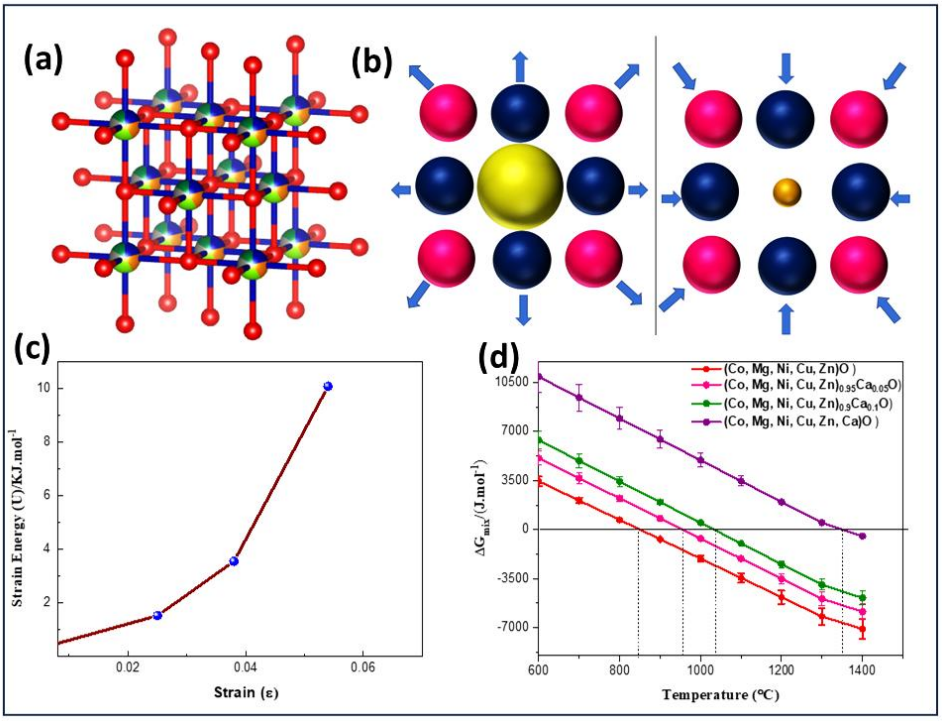

Figure 5.1 (a) Schematic showing the rocksalt crystal structure of HEO, (b) stress-induced in the lattice due to substitution of cation (yellow) with larger ionic radius (a) and with smaller ionic radii on host oxide system. Here blue and red spheres represent cation and oxygen as anions, respectively. (c) plot depicts the relationship between Gibbs free energy and temperature for the synthesis of single phase rocksalt structure (b) the relationship between strain energy vs strain due to ionic size mismatch.

To validate the estimated critical temperature, the five-component HEO (TM-HEO0) and Ca^{2+} substituted samples (TM-HEO5, TM-HEO10 and TM-HEO16) were synthesised by solution combustion methods and annealed to achieve a single phase. X-ray diffraction patterns were recorded after annealing at varying

temperatures in 100 °C intervals and analysed to examine the phase and structural parameters ((**Figure 5.2 (a, b)** and **Figure 5.3 (a-c)**).

Table 5.1 The estimated strain energy, enthalpy and critical temperature for single-phase formation.

Sample	E (Strain)	U (Strain Energy) kJ/mol	ΔH (Enthalpy) kJ/mol	ΔS (Entropy) J/k-mol	Critical Temp. (°C)
TM-HEO0	0	0	15	13.38	848
TM-HEO5	0.025	1.74	17.66	14.35	957
TM-HEO10	0.038	3.97	19.35	14.70	1043
TM-HEO16	0.064	10.94	24.27	14.87	1359

For sample having x=0.05, x=0.1 in $(Mg,Co,Ni,Cu,Zn)_{1-x}Ca_xO$ single-phase rock-salt (space group $Fm\bar{3}m$) is observed only after annealing at 1000 and 1100°C, which is close to our calculated values of 947 and 1043 °C, respectively (**Figure 5.2b** and **Figure 5.3c**). Below this critical temperature, other phases, in addition to the prominent rocksalt phase, are observed. Apart from rocksalt, tenorite (CuO), wurtzite (ZnO), and traces of intermediate $CaCuO_2$ phase are identified from XRD (**Figures 5.2a, 5.3a and 5.3b**). The presence of separate phases at temperatures lower than the critical temperature is attributed to the greater positive enthalpy (ΔH) than the negative TΔS term. On increasing the temperature above the estimated critical temperature, a single phase solid solution is observed.

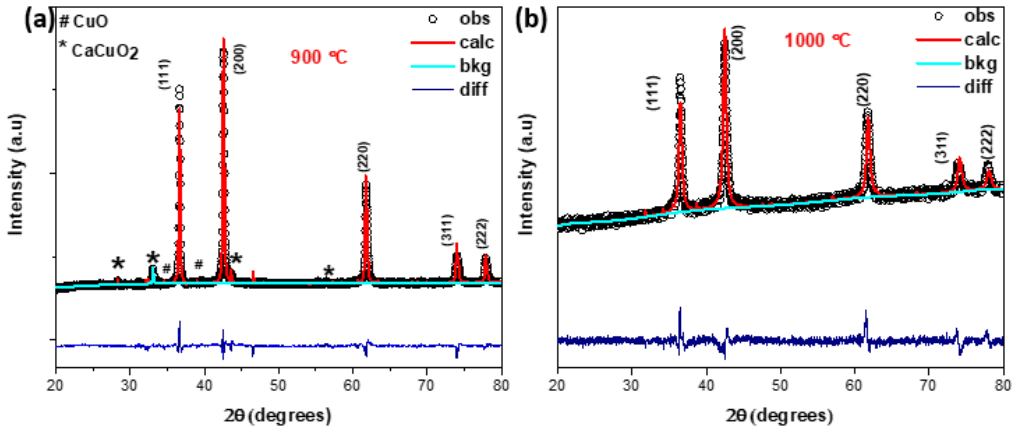

Figure 5.2 XRD pattern depicting phase evolution of (a) TM-HEO5 powder sample at a temperature (a) 900°C and (b) 1000°C respectively. Phase pure rocksalt structure obtained at 1000°C.

The estimated critical temperature for TM-HEO16 was 1359 °C; however, even after heating to 1400 °C, CaO peaks are observed, although the intensity of CaO peaks decreases significantly. The XRD pattern of TM-HEO16 annealed at different temperatures is shown in **Figure 5.4**. For TM-HEO16, apart from prominent peaks belonging to the rocksalt phase, there are minor peaks of CaO (estimated to be ~4 mole% from Rietveld analysis) present even after annealing at 1400 °C. Since the difference in ionic radius of Ca^{2+} ion and the average size of the cation in the host (Mg,Co,Ni,Cu,Zn)O HEO is 37.89%, which is much larger and can impose a solubility limit on Ca^{2+} in the parent TM-HEO0 [83]. This indicates that the solubility limit of Ca^{2+} is somewhere between 0.1 to 0.12 mole fraction.

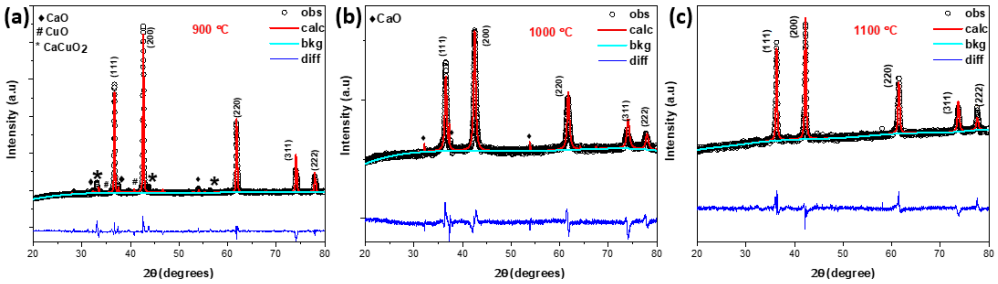

Figure 5.3 XRD pattern revealing phase evolution of TM-HEO10 powder sample at temperature (a) 900°C (b)1000°C and (c) 1100°C, respectively. Phase pure rocksalt structure obtained at 1100°C.

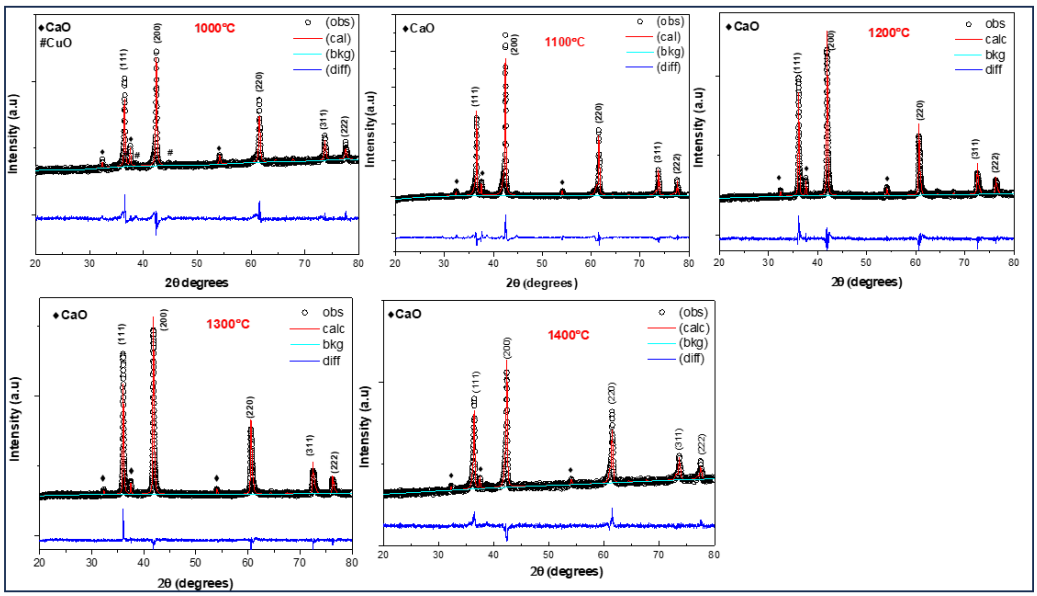

Figure 5.4 XRD pattern of equiatomic (Co, Mg, Ni, Cu, Zn, Ca)O (TM-HEO16) powder annealed at varying temperatures from 1000°C to 1400°C.

It is obvious from **Figure 5.5(a)** that the diffraction peaks shift to lower angles on increasing Ca^{2+} concentration, indicating lattice parameter increase, which is plotted in **Figure 5.5(b)**. The lattice parameter of the high entropy rocksalt phase was calculated from the XRD patterns. An increase in lattice parameter is observed

which follows a linear trend with the Ca^{2+} substitution. This shows that the interaction parameter for Ca^{2+} substitution in the HEO is rather small if not zero. The elemental mapping of all the samples using SEM-EDS, shown in **Figure 5.6**, confirms the random and uniform distribution of all constituent elements.

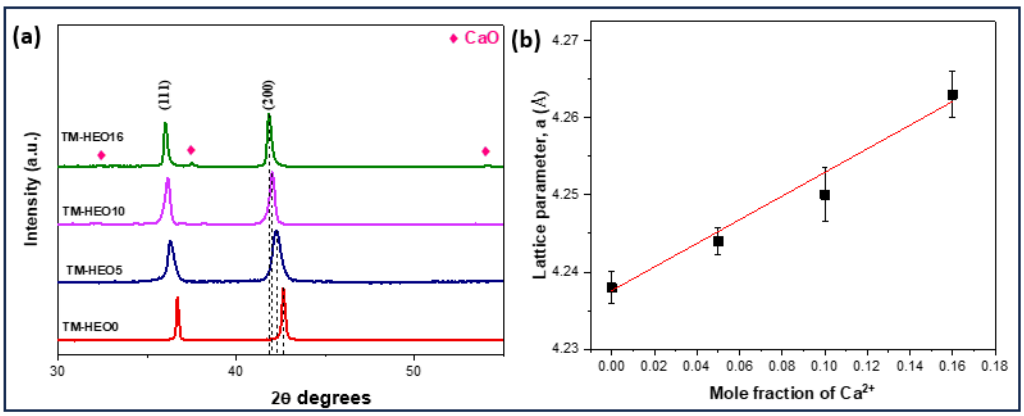

Figure 5.5 XRD pattern of powder sample of (a) five components HEO (TM-HEO0) and Ca^{2+} added $(Mg,Co,Ni,Cu,Zn)_{1-x}Ca_xO$ HEO at different compositions (x=0.05,0.10 and 0.16) at 900°C,1000°C,1100°C and 1400°C, respectively; (b) depicts the increase in lattice parameter as fraction of mole fraction of Ca^{2+}.

To confirm the phase purity and crystallinity of the synthesized samples, TEM analysis was performed at several spots. Representative images and SAED patterns are shown in **Figure 5.7, 5.8**, and **5.9** for TM-HEO0, TM-HEO5 and TM-HEO10, respectively. The bright field TEM images (**Figures 5.7a, 5.8a** and **5.9a**) and SAED patterns (**Figures 5.7c, 5.8c** and **5.9c**) confirm the phase purity and crystallinity.

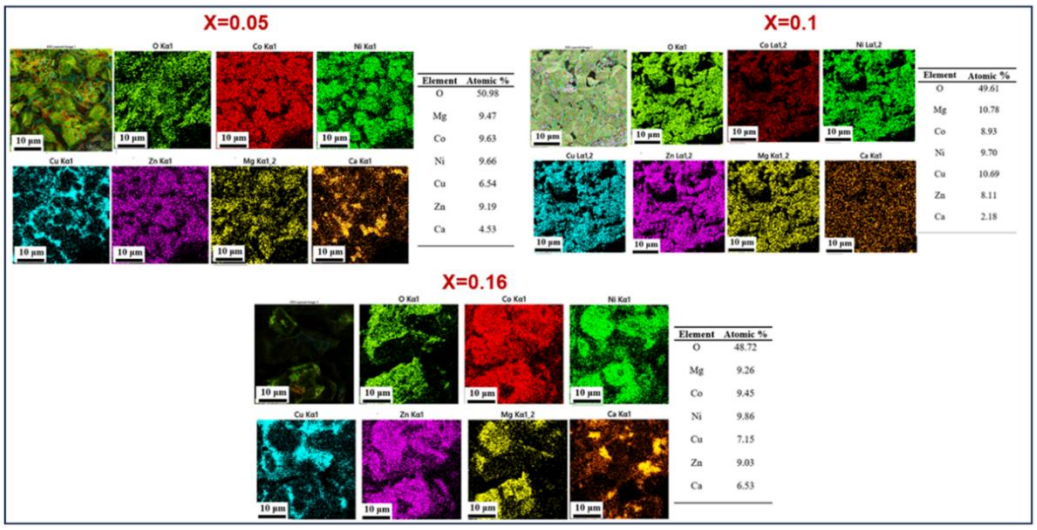

Figure 5.6 EDS and elemental mapping of the powder sample of TM-HEO5, TM-HEO10 and TM-HEO16 confirm uniform elemental distribution.

SAED in all the cases could be indexed to the rocksalt phase. **Figures 5.7b, 5.8b** and **5.9b** show the lattice fringes with inter-planar distances of 0.243, 0.245, and 0.249 nm in phase contrast image is attributed to (111) planes of rocksalt phase of sample TM-HEO0, TM-HEO5 and TM-HEO10, respectively.

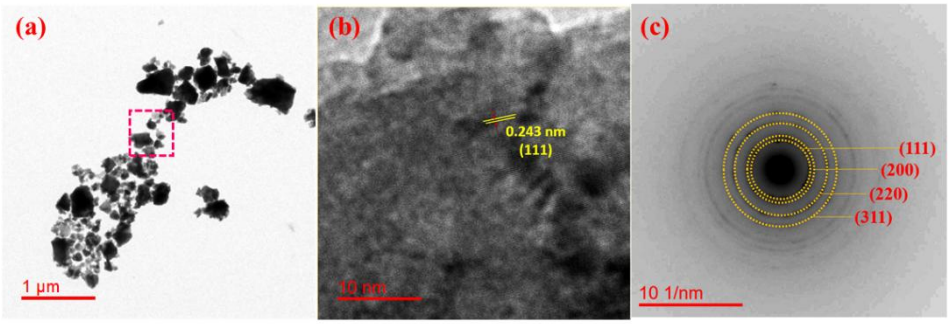

Figure 5.7 (a) Bright-field TEM image (b) phase contrast image showing interplanar distance 0.243 nm and (c) SAED pattern showing polycrystalline nature of TM-HEO0 sample.

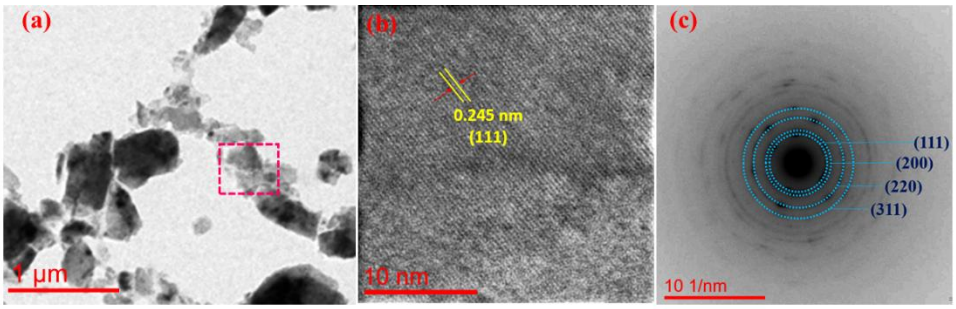

Figure 5.8 (a) Bright-field TEM image (b) phase contrast image showing inter-planar distance 0.245 nm and (c) SAED pattern showing polycrystalline nature of TM-HEO5 sample.

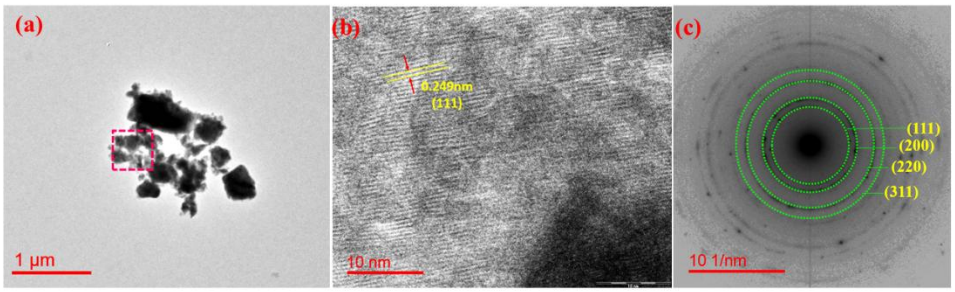

Figure 5.9 (a) Bright-field TEM image (b) phase contrast image showing interplanar distance 0.249 nm and (c) SAED pattern showing polycrystalline nature of TM-HEO10 sample.

5.3.2 Characterizing Distortion

In the rocksalt structure, each cation is surrounded by six anions in an octahedral symmetry. However, when Ca^{2+}, having a much larger size, is substituted into the lattice, it can cause distortions in the surrounding lattice [49,202,214]. These

distortions may cause the structure to deviate from the ideal rocksalt symmetry [115,149,215]. An equivalent structure with lower symmetry can be fitted (monoclinic in this case) for the rocksalt structure (**Figure 5.10**); at the same time, from the fitted rocksalt structure, a monoclinic unit cell can be derived mathematically [115,215].

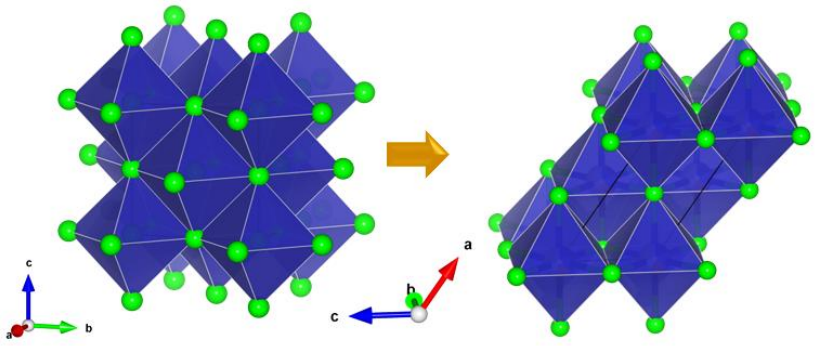

Figure 5.10 Schematic representation of strain-driven structural transition from rocksalt monoclinic structure.

It was hypothesised that if the rocksalt structure is ideal, the fitted monoclinic and mathematically derived monoclinic from the fitted rocksalt structure should conform [215]. However, in the case of distortion, the actual fitting and mathematically derived structure will not conform. In order to characterize the distortion, the fitted monoclinic structural parameters (**Figure 5.11**) were compared with the mathematically transformed monoclinic parameters. If there is no distortion, the monoclinic and rocksalt structures should give equivalent parameters. However, in the case of distortion, the transformed and fitted structures should show deviation. In a distorted rocksalt structure, the lattice parameter might change slightly, and the symmetry of the crystal structure may be reduced due to

the introduction of Ca^{2+}. Lamirand et al. [215] established that every cubic lattice can be converted into an equivalent monoclinic lattice, and the lattice parameters may be determined using trigonometric relationships as follows [216]:

$$a_m = \sqrt{6}\left(\frac{a_c}{2}\right) \quad (7)$$

$$b_m = c_m = \sqrt{2}\left(\frac{a_c}{2}\right) \quad (8)$$

$$\beta_0 = 125.264^{\circ} \quad (9)$$

where a_m , b_m , c_m, β_0 and are the monoclinic lattice parameters corresponding to cubic lattice parameters (a_c).

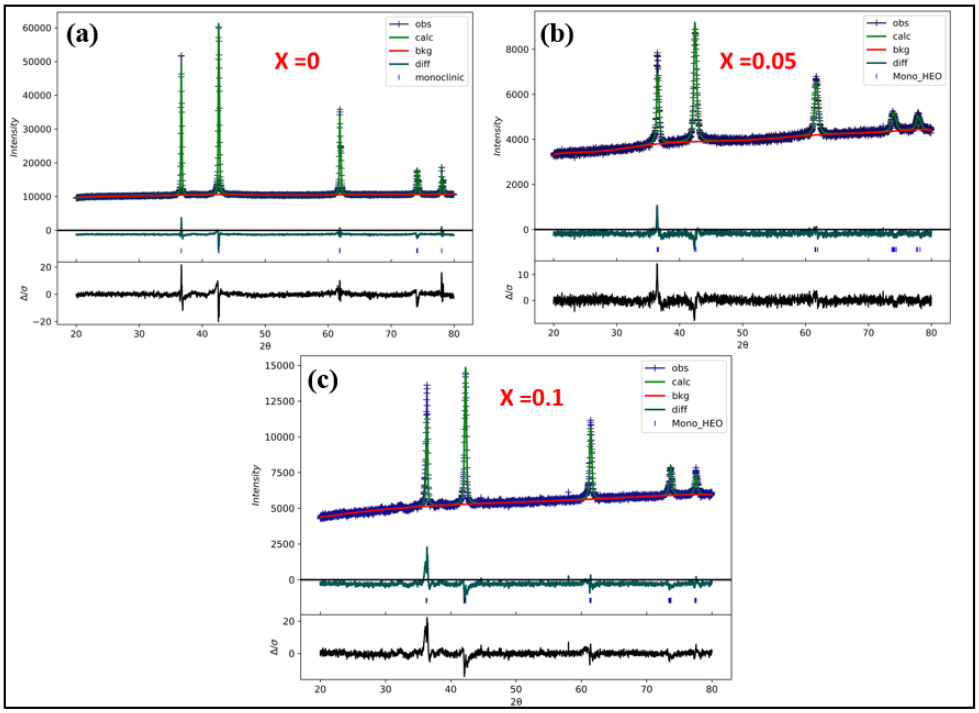

Figure 5.11 Rietveld refinement of the XRD spectra of (a) TM-HEO0 (b) TM-HEO5 (c) TM-HEO10 considering a monoclinic structure.

Assuming (Mg,Co,Ni,Cu,Zn)O system to be a pure rocksalt structure, the cubic lattice constant would be 4.237 Å, using trigonometric calculation the equivalent monoclinic lattice parameters were estimated to be a_m = 5.189 Å, b_m = 2.996 Å, c_m= 2.996 Å and β_0= 125.264°.

Table 5.2 Distortion percentage on Ca^{2+} addition in five component HEO.

Sample	Rocksalt (Fitted)	Monoclinic (Derived from Rocksalt)	Cell Vol.	Monoclinic (Fitted)	Cell Vol.	Distortion
	Lattice parameter (Å)	Lattice parameter (Å)	(Å^3)	Lattice parameter (Å)	(Å^3)	(%)
(Mg,Co,Ni,Cu,Zn)O (TM-HEO0)	4.237	a = 5.189 b= 2.996 c= 2.996 β = 125.264	38.059	a = 5.191 b= 2.998 c= 2.997 β = 125.259	38.083	0.065
(Mg,Co,Ni,Cu, Zn)$_{0.95}$Ca$_{0.05}$O (TM-HEO5)	4.244	a = 5.198 b= 3.00 c= 3.00 β = 125.264	38.197	a = 5.21 b= 3.0017 c= 3.009 β = 125.11	38.49	0.767
(Mg,Co,Ni,Cu, Zn)$_{0.9}$Ca$_{0.1}$O (TM-HEO10)	4.249	a = 5.204 b= 3.004 c= 3.004 β = 125.264	38.343	a = 5.219 b= 3.016 c= 3.01 β = 124.97	38.82	1.25

Any deviation in the calculated lattice parameters from the fitted values gives a clear indication of distortion from rocksalt structure [40, 41]. Rietveld refinement for all the samples, considering monoclinic symmetry, is shown in **Figure 5.10**, while fit values and the deviations in the parameters from that obtained mathematically are listed in **Table 5.2**. The deviation between the fitted and transformed lattice parameters increased with increased Ca^{2+} substitution which indicates an increase in structural distortion. Earlier studies attributed magnetostriction to the distortion due to Ca^{2+} substitution [115,150,215,217]; however, the present study shows that the strain-driven distortion can't be ignored in these oxide systems [19,147]. When Ca^{2+}, with its larger size, is substituted into the TM-HEO0 lattice, it can cause strain and distortions in the surrounding lattice. These distortions may lead the struture to deviate from the ideal rocksalt structure and become more similar to a distorted rocksalt or even a monoclinic structure.

Transmission electron microscopy (TEM) analysis was done to get a greater insight into the nature of distortion. **Figure 5.12(a,c)** depicts the TEM bright field of TM-HEO0, and Ca^{2+} added HEO with their corresponding SAED is shown in **Figure 5.12b** and **5.12d**, respectively. The diffraction pattern in **Figure 5.12b**, along the Z= $[1\bar{3}0]$ zone axis, confirms the rocksalt phase, with (002) and $(31\bar{1})$ plane *d*-spacings measuring ~2.07 Å and ~1.24 Å. These values closely match with the *d*-spacings of the TM-HEO0 as identified in the XRD pattern. Similarly, 10 mol.% Ca^{2+} substituted HEO (TM-HEO10), showing $(0\bar{2}0)$ and $(\bar{4}0\bar{2})$ plane along the zone axis of Z= $[\bar{1}02]$ having *d*-spacing 2.132 Å and 0.942 Å, respectively. A closer look into SAED patterns of Ca^{2+} substituted HEO (TM-HEO10) sample reveals that

principal reflections are arced with intensity modulation (marked with blue coloured dotted line) rather than being a circular spot. In addition, mottled contrast regions were also observed in the bright field TEM image of Ca^{2+} added HEO. This clearly indicates the distortion in the lattice.

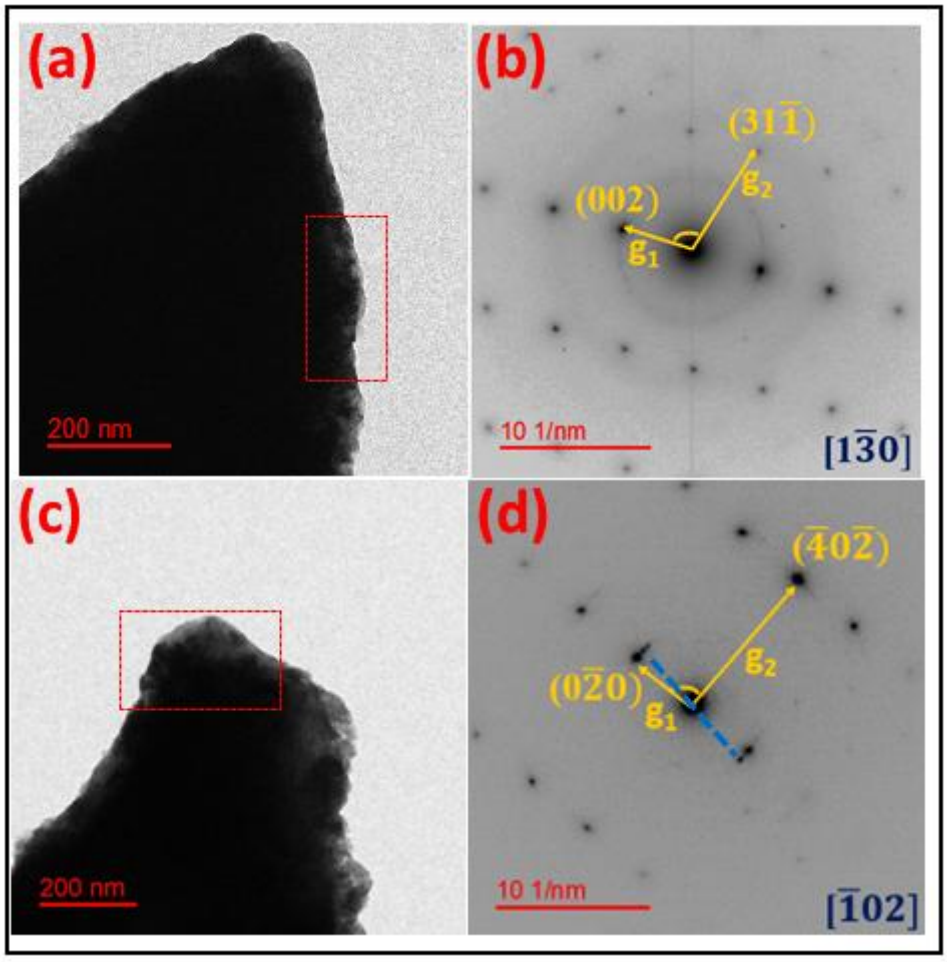

Figure 5.12 (a,c) TEM bright field image of TM-HEO0 and TM-HEO10 sample and their corresponding SAED along the Zone axis of Z= [1$\bar{3}$0] and Z= [$\bar{1}$02] respectively (c) intensity modulated arcing was observed (blue dotted line) indicate distortion in the TM-HEO10 sample.

A similar observation was made by Saptarshi et al., where mottled contrast regions in bright-field TEM images were attributed to the accumulated micro-strain in the lattice of quinary (Mg,Ca,Fe,Co,Ni)O HEO[147,218]. SAED pattern (along Z= [001]) corresponding to the mottled contrast region in the BF image (**Figure 5.13a**) reveals a 4-fold symmetry (**Figure 5.13b**). When intensity maxima in each arced spot in the diffraction pattern are joined, a slightly rotated square pattern with respect to the main square pattern is revealed, as shown with coloured dotted lines (**Figure 5.13b**). This indicates mutually rotated cubic domains around [001] direction [14]. **Figure 5.13c** shows a schematic of the arced principal reflection. Additionally, the high-resolution image of the mottled region shows fringes, which most likely, originated due to the twist strain in the lattice (**Figure 5.13d**) [219]. In the case of five component HEO (TM-HEO0), all the ions are of similar sizes (~0.7 Å), and the strain in the lattice is not enough to generate significant distortion. A schematic of the mutually rotated domains due to strain in the lattice of Ca^{2+} substituted samples is depicted in **Figure 5.13d.**

XPS analysis

Due to the ionic size mismatch, the Ca^{2+} incorporation results in lattice strain, which can drive the creation of vacancies [83,143] and some of the cations into the strain-induced valency change [220]. To characterize the vacancies and valence states of cations, XPS was carried out. The high-resolution Co *2p* spectrum (**Figure 5.14b**) unveiled the coexistence of Co^{2+} and Co^{3+} oxidation states.

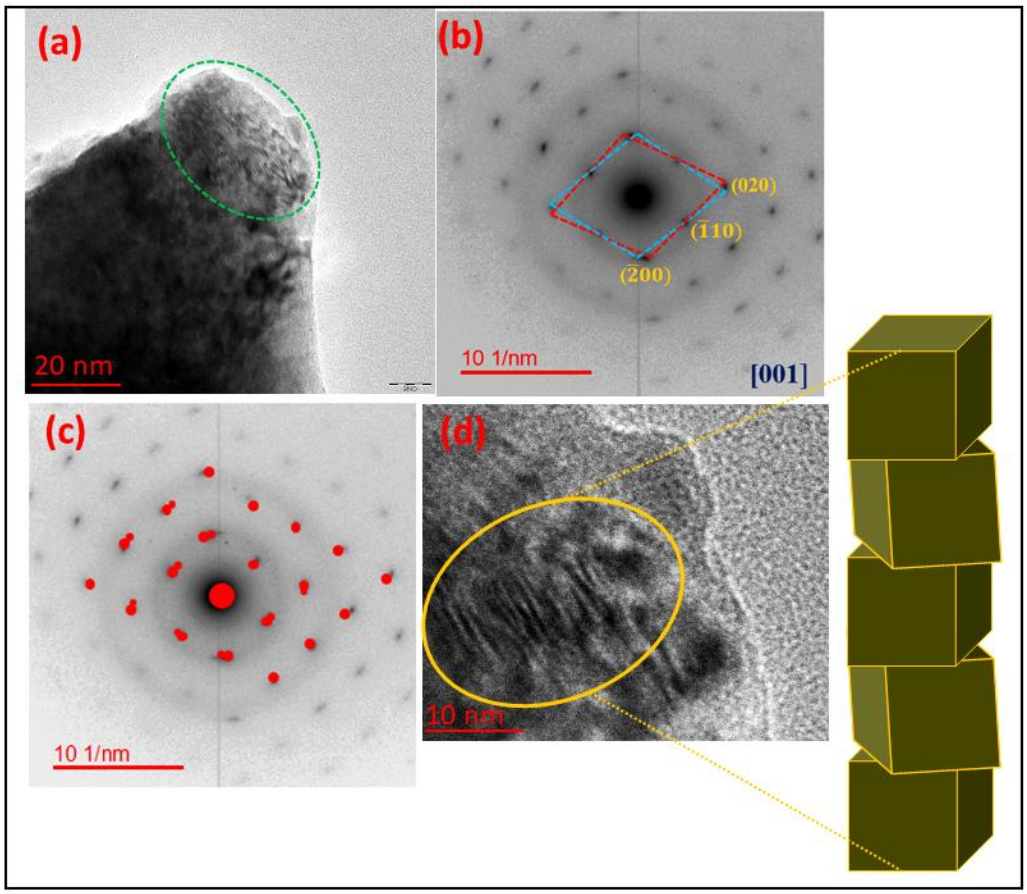

Figure 5.13 (a) Bright filed image of TM-HEO10 sample and (b) corresponding SAED along which indicate principal reflection being arced instead of spot. On joining the intensity maxima in each arced in the diffraction pattern, a small angle rotated square pattern with respect to the main pattern, as shown with coloured dotted line (red and blue), (c) schematic representing intensity modulated arcing in SAED pattern of TM-HEO10, (d) HR-TEM image showing fringe contrast in mottled region indicate mutually rotated cubic domains and thus signature of distortion in Ca^{2+} added Sample.

Spin-orbit doublets peaks at 782.4 eV and 797.7 eV correspond to Co^{2+}, while 780.4 eV and 796.3 eV signify Co^{3+}, highlighting the chemical complexity of the material.

$^{Co^{3+}}/_{Co^{2+}}$ ratio in TM-HEO0 is estimated to be 0.28 which increased to 0.72 for the Ca^{2+} added HEO (TM-HEO10) sample. The wide-scan Ni *2p* XPS spectrum for pure and Ca^{2+} substituted samples reveal the spin-orbital features of Ni^{2+} and Ni^{3+}. XPS peaks at 855.2 eV and 872.6 eV correspond to Ni^{2+}, while those at 856.2 eV and 875.2 eV is attributed to Ni^{3+}. The $^{Ni^{3+}}/_{Ni^{2+}}$ ratio in TM-HEO0 is 0.32, which increased to ~0.43 for TM-HEO10 sample (**Figure 5.15a**). A weaker peak at 851.4 eV in TM-HEO0 was attributed to the presence of small amounts of metallic Ni. Similarly, the Cu *2p* spectrum (shown in **Figure 5.15b**) could be deconvoluted into peaks at 933.6 eV and 954.2 eV (attributed Cu^{2+}) and at 932.7 eV and 952.8 eV (attributed Cu^{1+}). For TM-HEO0, $^{Cu^{1+}}/_{Cu^{2+}}$ ratio is 0.23 which increases to 0.53 for TM-HEO10.

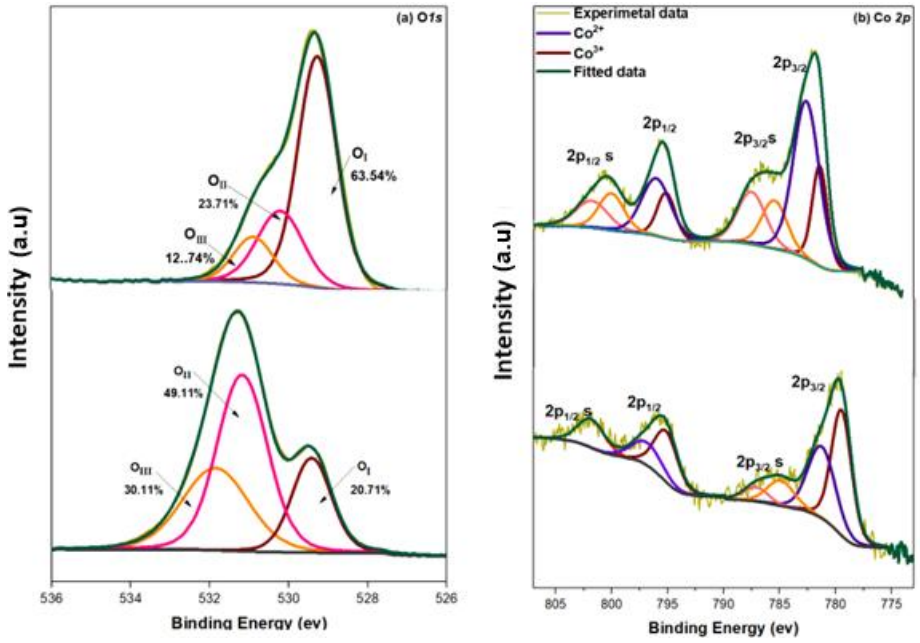

Figure 5.14 High resolution XPS spectra of (a) O1s (b) Co 2p of TM-HEO0 (above) and TM-HEO10 (Below) indicating that accommodating large size of Ca^{2+} by enhancing oxygen deficit site and oxidation of Co^{2+}.

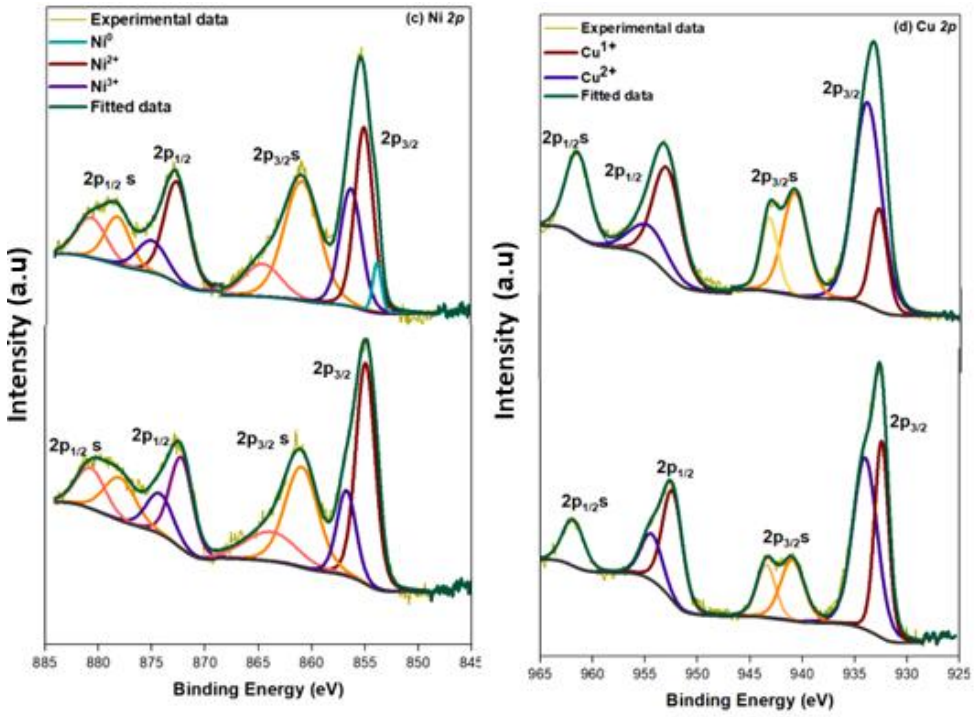

Figure 5.15 High resolution XPS spectra of (a) Ni 2p (b) Cu 2p of TM-HEO0 (above) and TM- HEO10 (below).

The metal cation going into a lower valence state supports creation of oxygen vacancies in the lattice[114]. **Table 5.3** summarizes the ratio of the different valence states of Co, Ni, Cu in both samples. Further, The Ca^{2+} *2p* spectrum features spin-orbit split peaks at 347.01 eV ($2p_{1/2}$) and 350.57 eV ($2p_{1/2}$), along with a *MgKLL* auger peak (349.04 eV) confirming Mg^{2+} presence [143]. The Zn 2p scan reveals peaks at 1021.37 eV ($2p_{3/2}$) and 1044.46 eV ($2p_{1/2}$), consistent with Zn^{2+} with nearly identical spectra in both the sample samples.

Table 5.3 The ratio of different valence state of Co,Ni,Cu in TM-HEO0, TM-HEO10.

Sample	Co^{3+}/Co^{2+}	Ni^{3+}/Ni^{2+}	Cu^{1+}/Co^{2+}
TM-HEO0	0.28	0.32	0.23
TM-HEO10	0.72	0.43	0.53

EXAFS analysis

To unravel the local structural environment around Co, Ni, Zn, and Cu in the TM-HEO0 and TM-HEO10 sample, extended X-ray absorption fine structure (EXAFS) analysis (**Figure 5.16**) was carried out. Due to beamline energy limitations, the Mg^{2+} and Ca^{2+} K-edge absorption spectrum could not be collected, while due to the absorption edge position of Co, Ni Cu and Zn EXAFS data were truncated around 12 $Å^{-1}$ to avoid interference from adjacent absorber edges [96].

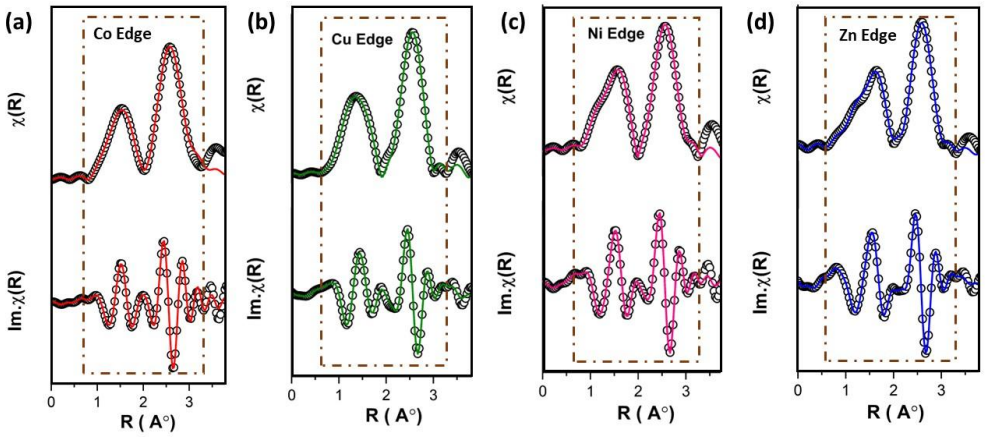

Figure 5.16 Data and fits for the FT of k^2 χ(k), denoted χ (R), and their respective imaginary parts (Im.χ (R)) for (A) Co, (B) Cu, (C) Ni, and (D) Zn for TM-HEO10 sample. The fit window range is outlined in dark brown colour (dash line).

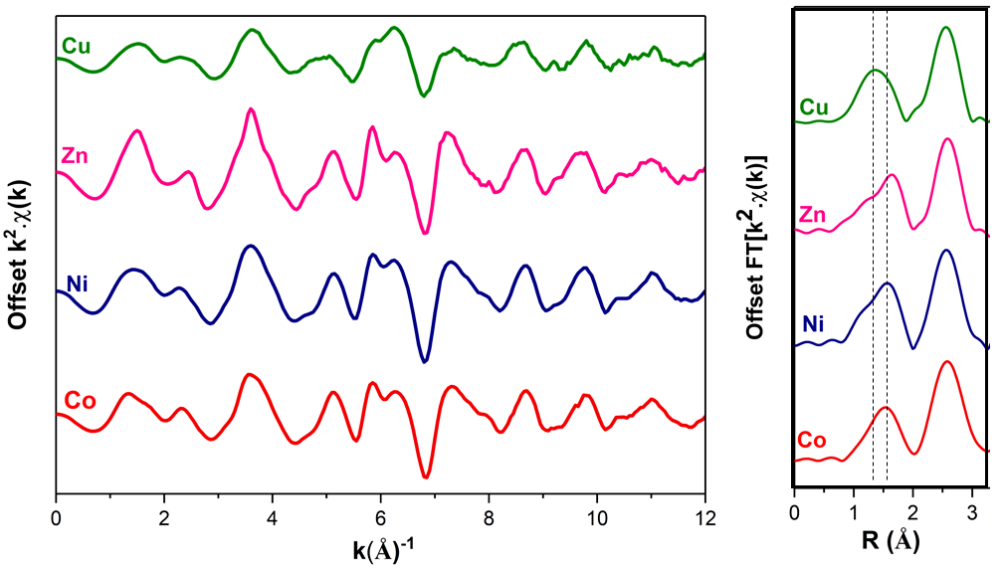

Figure 5.17 $k^2\chi(k)$ EXAFS spectra plot for Co, Ni, Zn, Cu absorbers in Ca^{2+} added sample (TM-HEO10) at 1100°C and corresponding Fourier transform of $k^2\chi(k)$ in the range of 0 to 3 Å. First shell peak around Co, Ni, Zn almost similar except for Cu for which peak is shifted marginally to lower R. For the second shell peaks are almost similar for all the absorber.

Figure 5.17 presents the weighted EXAFS spectra of TM-HEO10 in k-space, revealing that Co, Ni, and Zn have similar short-range environments, indicative of a uniform cation distribution within the lattice. Cu, however, shows deviations attributed to the Jahn-Teller (J-T) type distortion [144,146]. Fourier transform (FT) of the $k^2\chi(k)$ data in the Hanning window 3.25–11.9 Å revealed two prominent peaks between 1–3 Å, corresponding to the first coordination shell (metal-oxygen interactions) and the second coordination shell (metal-metal interactions), respectively. Notably, phase shift corrections indicate an approximate true scattering distance offset of 0.5 Å, with detection limits for scattering length

fluctuations constrained to ~0.15 Å (approximately given by ~$\pi/2\Delta k$) [198]. EXAFS fitting results highlight a systematic shift in both the first and second coordination shells towards larger scattering distances in TM-HEO10 compared to TM-HEO0, in agreement with the observed lattice parameter increase from XRD. Co, Ni, and Zn are found to maintain a nearly identical environment, consistent with a regular octahedral coordination model involving six oxygen ions. Cu does not conform to this model due to its J-T distortion, which results in different bond lengths for four planar and two axial oxygen ions in the octahedral symmetry [96]. **Figure 5.16** shows first shell peaks of Co, Ni, Zn are almost similar except for Cu for which the peak is shifted marginally to lower R. Further when EXAFS plot in Co-K edge of TM-HEO10 compared to that of TM-HEO0, it was observed that first shell (M-O) and second shell (M-M) peaks is slightly suppressed in the case of TM-HEO10 (shown in **Figure 5.18**) indicating the presence of vacancies which was also confirmed by surface level characterization XPS. Cu -K edge spectra show suppressed peak in second shell (M-M) coordination of TM-HEO10 indicating electron rich site near Cu and thus reduces its valency to Cu^{1+} as confirmed by XPS also.

These findings are summarized in **Table 5.4** listing the key fitting parameters such as amplitude reduction factor (σ^2), and scattering path distances (R). From the **Table 5.4**, it is clear that bond distances increased for Co, Cu and Zn for the both shells. In the case of Ni, a marginal change in bond length is noticed, which indicates distortion around Co, Cu, and Zn is more prominent compared to Ni.

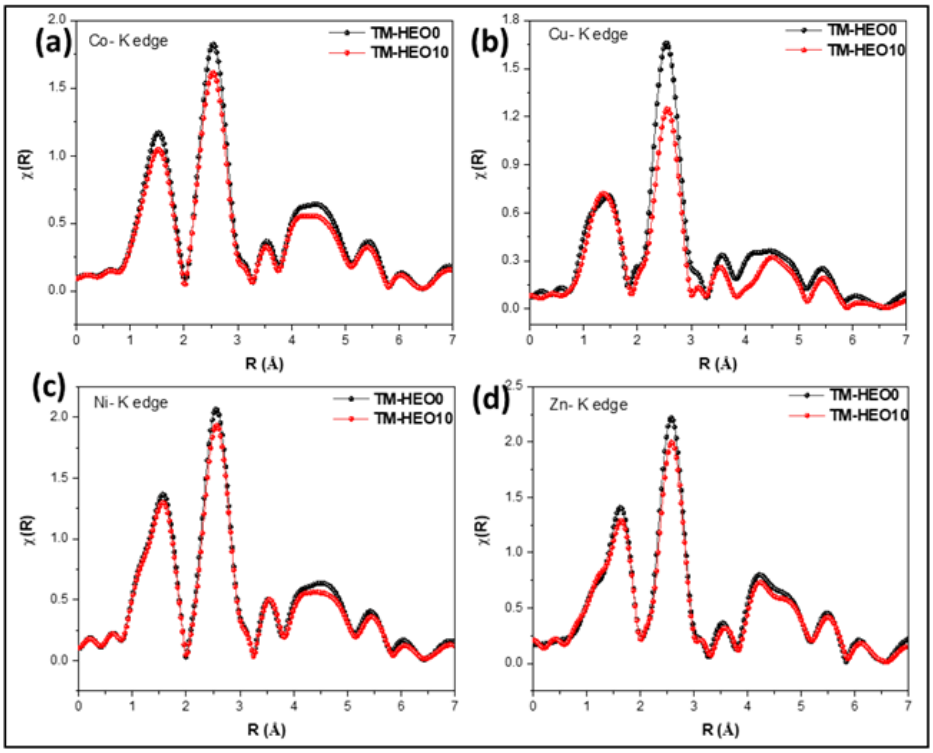

Figure 5.18 Comparison of FT of k^2 χ(k) plot for TM- HEO0 and TM-HEO10. suppression of peak intensity in TM-HEO10 indicates distortion in Ca^{2+} added sample.

Microstructural analysis

The grain morphology of TM-HEO10 and TM-HEO pallet sample sintered at 1100°C for 4h was analyzed using SEM (images are shown in **Figure 5.19**). A high relative density in the range of 91-93% without intergranular pores is obtained for both the sample. A larger grain sizes were observed in Ca^{2+} added TM-HEO-10 sample when compared to TM-HEO0. The mean grain size (G) of sintered TM-HE00 and TM-HEO10 pellets, analyzed through ImageJ software, were 3.9 μm and 7.2 μm, respectively (inset). The increase in mean grain size in the Ca^{2+} added sample was attributed to the fact that when cations with larger size replace smaller

host cations, it causes lattice strain. The strain fields promote the formation and migration of defects such as vacancies and interstitials, which help in atomic diffusion [221,222]. Diffusion mechanisms are crucial for sintering, as they allow atoms to move and rearrange to reduce total energy, which helps in mass transport during sintering and enhances grain growth. A thicker grain boundary is observed in the case of TMH-HEO10 which is ascribed to defect segregation around the boundary region.

Table 5.4 EXAFS fitting results for Co, Ni, Zn, and Cu in TM-HEO10

				TM-HEO0		TM-HEO10	
Absorber	Shell	Scatterer	N	σ^2 (Å^2)	R (Å)	σ^2 (Å^2)	R (Å)
Co	1	O	6	0.01407	2.0999	0.00530	2.1209
	2	Co	2	0.02088	2.97809	0.01398	2.9981
		Ni	3				
		Cu	3				
		Zn	2				
		Mg	2				
Ni	1	O	6	0.00873	2.07188	0.0089	2.07188
	2	Co	2	0.01337	2.98004	0.0199	2.99544
		Ni	2				
		Cu	3				
		Zn	3				
		Mg	2				
Cu	1	O	4	0.01529	1.9885	0.01	1.995
	1	O	2		2.2358		2.2574
	2	Co	2	0.02956	2.98902	0.0278	2.9932
		Ni	2				
		Cu	2				
		Zn	3				
		Mg	3				
Zn	1	O	6	0.01306	2.11996	0.0123	2.1396
	2	Co	3	0.00778	2.99804	0.0197	3.0258
		Ni	2				
		Cu	2				
		Zn	2				
		Mg	3				

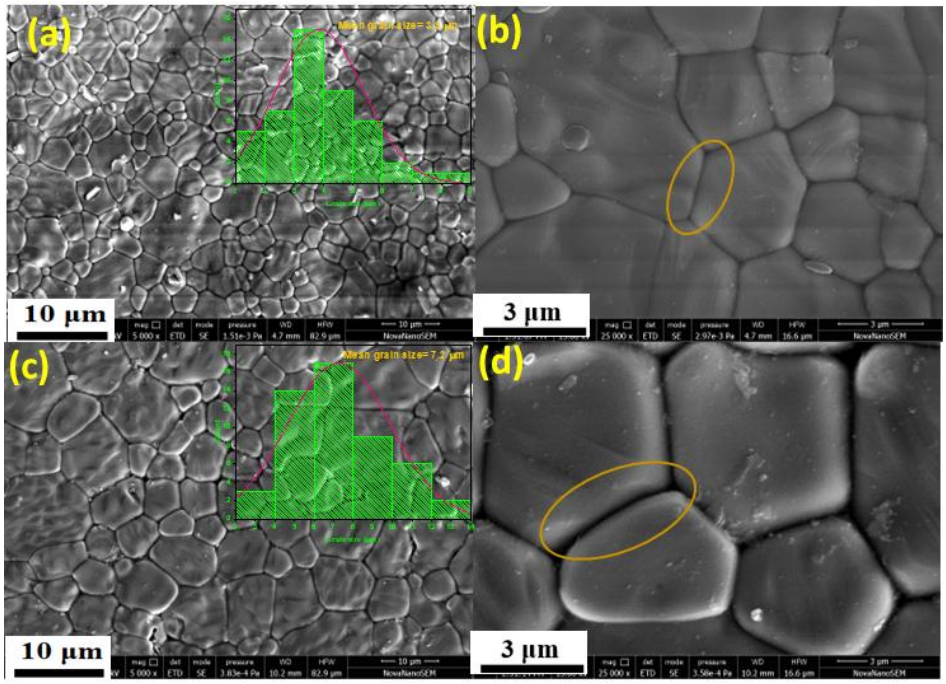

Figure 5.19 FE-SEM image of grain size of TM-HEO0 and TEM10 pallet sintered at 1100 °C 4hr.The obtained relative density was in the range of 93-95% for both the sample and the estimated mean grain size (in inset) of the TM-HEO0 and TM-HEO10 sintered pallet was 3.9 µm and 7.2 µm respectively.

Generally, ion diffusion aids the mass transport across GB which results in grain growth in polycrystalline ceramics [223–225]. addition of Ca^{2+} increased O_V as confirmed by XPS discussed in the earlier section, which supports GB mobility and thus grain growth.

5.3.3 Electrical properties

Dielectric properties

Frequency dependent dielectric property of sintered TM-HEO0 and TM-HEO10 samples are shown in **Figure 5.20(a-d)**. The dispersion behavior of the real part of

the dielectric constant shows typical behaviour of dielectric oxides. The real part of the dielectric constant or permittivity was estimated using the relation [226,227]:

$$\varepsilon_r' = \frac{C_p * d}{\varepsilon_0 A} \qquad (10)$$

where C_p is the capacitance, ε_0 is permittivity at vacuum, d is the thickness and A be the area of the sample. At lower frequencies, the dielectric constant is greater and decreases with the rise in the frequency of the applied external electric field for both samples as shown in **Figure 5.20(a b)** which is attributed to the extrinsic (space charge, grains, and grain boundaries) and the intrinsic contribution (ionic, dipolar, and electronic) to the dielectric polarization [223]. Relaxation of extrinsic elements and each type of polarization has a characteristic relaxation frequency above which its effectiveness diminished and thus causes a reduction in dielectric constant with increasing frequency. The high dielectric constant at low frequencies is ascribed to the Maxwell-Wagner type of interfacial polarization [2,59]. The measured dielectric constant is 2992 and 3237 for TM-HEO0 and TM-HEO10, respectively. The increase in the dielectric constant of the Ca^{2+} substituted sample is directly connected to the space charge polarization. Defects such as vacancies, interstitials, grain boundaries and the trap states which capture the surface charge are known to enhance the space charge polarization. The substitution of Ca^{2+} results in the creation of vacancies and multivalent cations as a part of geometrical compensation for distortion (as confirmed by XPS). The electron hopping between multiple ions, including Co^{2+}/Co^{3+}, Ni^{2+}/Ni^{3+} and Cu^{2+}/Cu^{1+}, facilitates charge

carrier movement locally along the applied field [25,160,226,228,229]. Charge carriers aligning along the direction of the applied field exhibiting

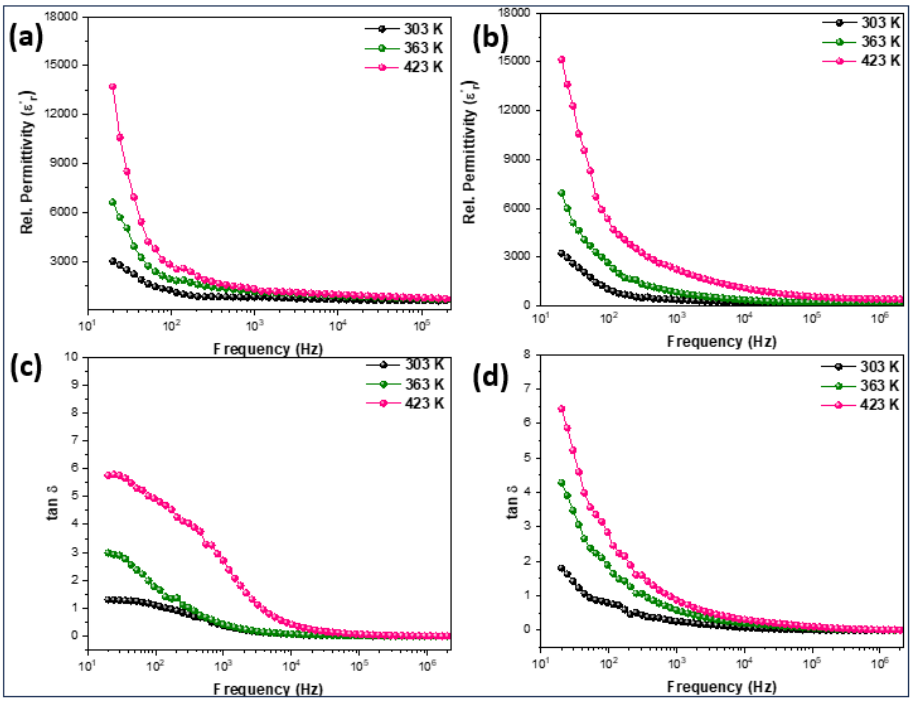

Figure 5.20 Frequency dependent relative permittivity, dielectric loss, and conductivity plot at different temperature for (a,b,c) TM-HEO0 and (d,e,f) TM-HEO10.

both ionic and orientation polarization, which facilitates charge accumulation at GB enhancing the dielectric constant. Apart from this, another reason for the observed greater dielectric constant in TM-HEO10 is the distortion which increases the scattering of charge carriers reducing the mobility, thus hindering the carrier flow, resulting in increased accumulation of charged carriers at the distortion domain boundaries which increases the dielectric constant. **Figure 5.20(a & b)** depicts the frequency-dependent dielectric constant at varying temperatures for TM-HEO0 and

TM-HEO10. It is clear the ε_r' progressively increases with temperature. The reason for this temperature dependence is ascribed to thermal mobility, which assists in ion jump and space charge polarization. Further, the measurement of energy loss is represented by the dielectric loss factor (tan δ), which may be calculated as tan δ = $\varepsilon_r''/\varepsilon_r'$, where ε_r'' is the imaginary component of the complex dielectric constant and angle δ is the phase difference between the applied electric field and the current. Dielectric loss happens when the polarization lags behind the applied alternating field [39,230]. This mostly occurs as a result of the impact of grain boundaries, impurities (doping), and crystalline flaws. Apart from this density of ceramic materials also plays a vital role in regulating dielectric loss. In this case, the density of both samples was nearly the same therefore, the effect of density on dielectric loss is discounted.

Table 5.5 Dielectric constant (ε_r'), dielectric loss (Tan δ), and conductivity (σ) at room tempearature.

Sample	**Dielectric constant (ε_r')**	**Dielectric loss (Tan δ)**	**Conductivity (σ) (S/cm)**
TM-HEO0	2992	1.3	$5x10^{-8}$
TM-HEO10	3237	1.8	1.7×10^{-7}

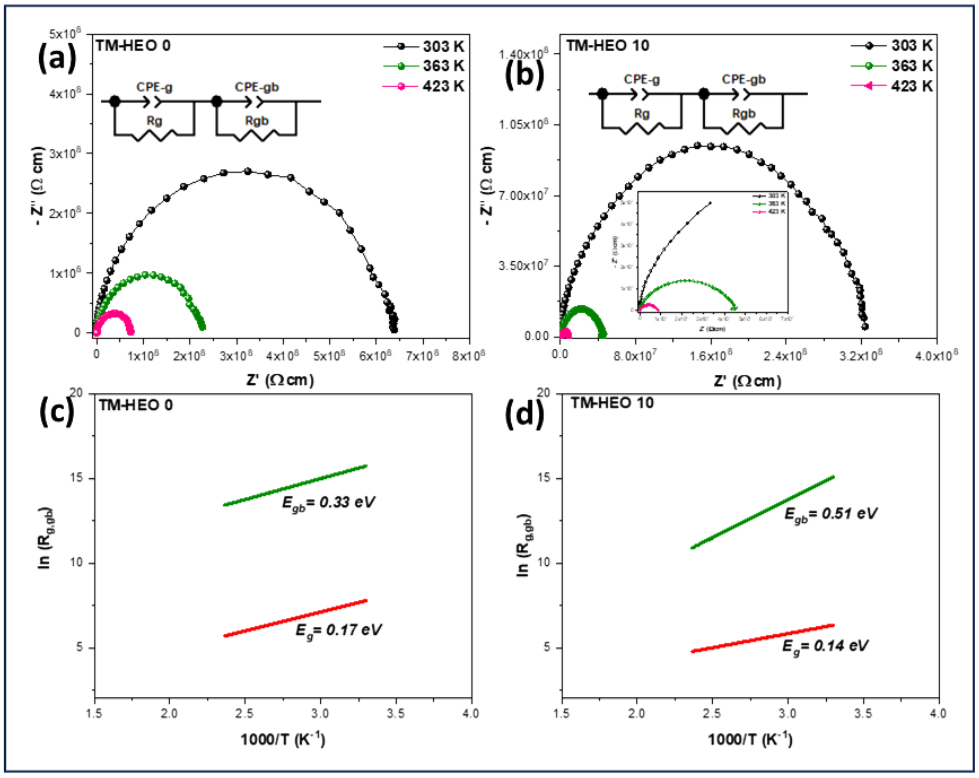

Figure 5.21 The Nyquist plot of the (a) TM-HEO0 and (b)TM-HEO10 pallet samples at different temperatures. Arrhenius plot ionic conductivity plot for (c) TM-HEO0 and (d) TM-HEO10 indicating grain boundary activation energy (E_{gb}) of 0.33 eV and 0.51 eV, respectively.

Frequency-dependent loss value at different temperatures is shown in **Figure 5.20(c,d)**. It is obvious that dielectric loss increased marginally in TM-HEO10, which is attributed to the increase in charge carrier concentration causing ion migration loss. This includes combined effect of conduction losses; ion jump and dipole relaxation losses. Conduction losses are directly related to conductivity which give rise to current with ac field in phase with applied electric field and thus

causes dielectric loss. **Table 5.5** showing dielectric constant and dielectric loss at room temperature. Further, similar to dielectric constant, dielectric loss also shows direct relation with temperature as a greater number of charge carriers are thermally activated, these charge carriers dissipate energy when moving through the material in response to an alternating electric field, which contributes to dielectric loss. Moreover, increase in dielectric loss on increasing temperature also attributed to rise in conduction loss. The Impedance spectroscopy for the polycrystalline material determines the GB resistance (R_{gb}) through the diameter of large semicircle arc in impedance complex plane (Z^*) as shown in **Figure 5.21 (a & b)**. To explain the Nyquist plot, circuit diagram with constant phase element (CPE) and resistance (R) for grain (denoted as CPE-g and R_g) and grain boundary (denoted as CPE-gb and R_{gb}) was fitted. By examining the impedance complex Z* plot at 303 K for both the samples it was noticed that reduced low frequency tangent loss for TM-HEO0 is due to the increase in $R_{gb.}$ The relationship between tan δ and R_{gb} for the polycrystalline ceramic can be effectively described by the following relation [226,229].

$$tan\ \delta \simeq \frac{1}{\omega \varepsilon_0\, \varepsilon\prime C_0 R_{gb}} \qquad (11)$$

where ε_0 and C_0 represent the permittivity and capacitance of free space (8.854 × 10^{-12} F/m), respectively and thus implies that low frequency loss tangent has inverse relation with $R_{gb.}$ Increased dielectric loss in Ca^{2+} added sample also related to its lower grain boundary resistance (R_{gb} ~3.2 MΩ) compared to TM-HEO0 (R_{gb} ~ 6.5MΩ). Lowering of grain boundary resistance ascribe to decrease in potential barrier hight (ϕ_b) at grain boundary due to increase in charge carrier concentration

in grains. Further, the nonzero intercept value on the Z'-axis at high frequencies signifies the grain resistance (R_g), highlighting the semiconducting nature of the grain. R_g at the room temperature for the TM-HEO0 and TM-HEO10 sintered sample was estimated to be 2124.3 Ω and 556 Ω, respectively. R_g for TM-HEO10 sample is ~4 times lower when compared to TM-HEO0 sample. The activation energy for transport along the grain and grain boundary was estimated using the Arrhenius equation [129,140,231].

$$R_{g,gb} = R_0 e^{\left(\frac{E_{g,gb}}{k_b T}\right)} \qquad (12)$$

where R_0 is the pre-exponential term, T being the absolute temperature, while E_g and E_{gb} represent activation energy of grain and grain boundary, respectively. From the above relation, the calculated E_g for TM-HEO0 and TM-HEO10 samples are 0.17 eV, and 0.14 eV, while corresponding E_{gb} are 0.33 eV, and 0.51 eV, respectively (fit is shown in **Figure 5.21 (c,d)**). **Table 5.6** lists the grain, grain boundary resistance and corresponding activation energy. The significant difference between E_g and E_{gb} supports the IBLC effect in both the HEO sample, specifying semiconducting grain and insulating grain boundary. In Ca^{2+} added sample has a greater E_{gb} indicating an enhanced potential barrier at GB which means the conduction is mainly through the grain.

Table 5.6 Grain (R_g) and grain boundary resistance (R_{gb}) and corresponding activation energy.

Sample	R_g(MΩ)	R_{gb} (MΩ)	E_g	E_{gb}
TM-HEO0	0.02	6.25	0.17	0.33
TM-HEO10	0.005	3.2	0.14	0.51

AC conductivity

Frequency dependent ac conductivity of both sintered TM-HEO0 and TM-HEO10 samples at different temperatures (shown in **Figure 5.22 (a&b)**) were estimated using the relation [59,232]

$$\sigma_{ac} = \omega^2 \varepsilon_0 \varepsilon_r' \tan \delta \qquad (13)$$

The ac conductivity of Ca^{2+} substituted sample was greater by an order of 10 in magnitude at lower frequency range 10 Hz to 1 kHz when compared with undoped HEO. **Table 5.5** shows the conductivity for both samples at room temperature. It is interesting to note that there are two regions that depict the conductance of TM-HEO0. At lower frequency region, conductivity increased gradually, but at high frequencies there is abrupt increase in conductivity. However, no slope change is observed in the case of TM-HEO10, and there is a gradual increase at all frequency range.

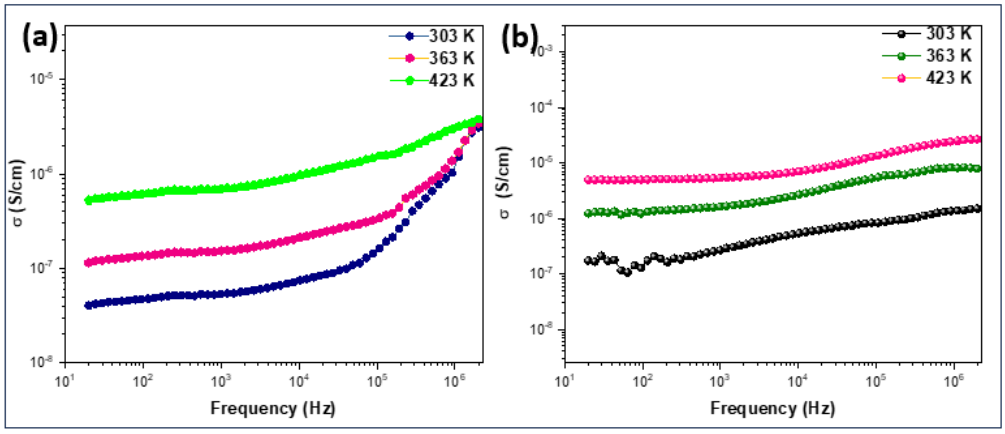

Figure 5.22 Frequency dependent conductivity plot at different temperature for (a) TM-HEO0 and (b) TM-HEO10.

The ac conductivity of both samples is ascribed to the frequency exponent of the mobile ions (n) in the Jonscher power law which is given by [225]:

$$\sigma_T = \sigma_{DC} + A\omega^n \qquad (14)$$

where σ_T is total conductivity, and A is pre factor depends on material property. The value of n estimated from the ln σ_{ac} vs ln ω plot as depiected in **Figure 5.23.** It was observed that the exponent n decreses with increasing temperature. This indicates to the correlated barrier hopping (CBH) mechanism of conduction in both samples [233,234], which suggest ac conductivity is largely controlled by charge carriers hopping in tandem with lattice distortion or poloron [235,236]. The surge in the conducitvity of TM-HEO10 is linked to the defect generation such as oxyegen vacancy and at the same time oxidation of multivalent cation as discussed in XPS analysis section .

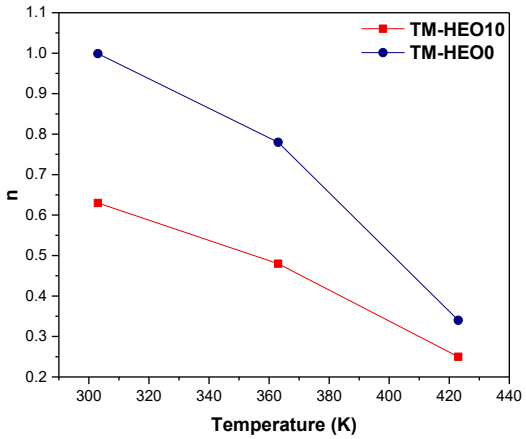

Figure 5.23 The exponent n in Jonscher power law indication CBH model best describe the conduction behaviour.

These defects create free carriers that interact with strain fields, particularly around vacancies, and form small polarons [236]. This polaron hopping primarily drives conductivity in Ca^{2+} added sample, The increased defect density and free carriers in Ca^{2+} added samples not only elevate DC conductivity but also facilitate polaron hopping, further supporting AC conductivity at elevated frequencies. In contrast, undoped TM-HEO0 sample start with initial defects, leading to fewer free carriers and thus indicating lower DC conductivity, which only increases with temperature and AC conductivity takes over at higher frequencies, typically $>10^4$ Hz, driven by polaron hopping.

5.4 Conclusions

A formulation for accounting the strain energy for the dissolution of larger isovalent cation into high entropy phase formation is proposed and validated by substituting Ca^{2+} in (Mg,Co,Ni,Cu,Zn)O. The strain due to the large size of the Ca^{2+} caused a

larger activation energy barrier, for the formation of single-phase rocksalt solid solution $(Mg,Co,Ni,Cu,Zn)_{1-x}Ca_xO$, which enhanced the critical temperature for entropic stabilization (TΔS). The critical temperature for single-phase solution phase formation increased from 875 ℃ for (Mg,Co,Ni,Cu,Zn) O to 1000 and 1100 °C for $(Mg,Co,Ni,Cu,Zn)_{0.95}Ca_{0.05}O$ and $(Mg,Co,Ni,Cu,Zn)_{0.9}Ca_{0.1}O$. In the case of equimolar six-component (Mg,Co,Ni,Cu,Zn,Ca) O HEO, although the critical estimated temperature was 1359 ℃, even after heating to 1400 ℃ only about 0.12 mole fraction of Ca^{2+} could be dissolved, indicating to the solubility limit imposed by the large cationic size difference. Further the large size of Ca^{2+} incorporation causes strain driven structural deviation from the ideal rocksalt structure is as confirmed by electron microscopy. The large size of Ca^{2+} when incorporated in five component (Mg,Co,Ni,Cu,Zn) O creates under co-ordinated oxygen and drives oxidation of multivalent element in lattice. Due to the structural distortion and defect creation, Ca^{2+} added sample exhibits a greater dielectric constant and conductivity when compared to five component HEO.